Atomic-resolution annular dark-field STEM image calculations

K. Watanabe,[1] T. Yamazaki,[2] I. Hashimoto,[2] and M. Shiojiri[3,4]
[1]*Tokyo Metropolitan College of Technology, 1-10-40 Higashiohi, Tokyo 140-0011, Japan*
[2]*Department of Physics, Science University of Tokyo, Tokyo 162-8601, Japan*
[3]*Department of Anatomy, Kanazawa Medical University, Ishikawa 920-0293, Japan*
[4]*Kyoto Institute of Technology, Kyoto 606-8585, Japan*
(Received 9 November 2000; revised manuscript received 28 March 2001; published 31 August 2001)

A method based on the three-dimensional Bloch wave description has been developed for the simulation of atomic-resolution annular dark-field (ADF) scanning transmission electron microscopy (STEM) images, which includes the coherent Bragg reflection and the incoherent thermal diffuse scattering (TDS). The contribution of TDS is estimated using two kinds of optical potentials. The validity and accuracy of the method are demonstrated by comparisons in focus dependence between experimental and calculated high-angle (HA) ADF STEM images and in thickness dependence between experimental and calculated ADF STEM intensities. The method reduces the computing time for a HAADF STEM image calculation to about one-tenth of that required for the usual three-dimensional Bloch wave method.

DOI: 10.1103/PhysRevB.64.115432 PACS number(s): 68.37.Lp, 61.66.−f

I. INTRODUCTION

High-resolution transmission electron microscopy (HRTEM) has been widely known as the most valuable tool to visualize atomic structures. As is well known, the analysis of HRTEM images needs image simulation because they do not generally exhibit the real atomic structures owing to the phase effect by lens aberration and focus and the dynamical effect. In the 1970s, high-resolution scanning transmission electron microscopy (STEM) made it possible to image individual atoms, using a low-angle annular dark-field (LAADF) detector to collect scattered electrons from heavy atoms.[1] This imaging mode, however, has a disadvantage in that the LAADF imaging is mainly due to strong dynamical diffraction so that the intensity does not always depend on atomic number. The use of a high-angle (HA) ADF detector reduces the detection of coherent Bragg reflection and increases that of the incoherent thermal diffuse scattering (TDS).[2] Resultant incoherent images exhibit strong intensity dependence on atomic number.

Since Kirkland, Loane, and Silcox[3] reported that ADF STEM can identify single gold atoms on a Si(111) substrate, many investigations have reported the effects of focus, thickness, and inner detector angle on its imaging.[4–11] Pennycook and Jesson[4] proposed that HAADF STEM provides incoherent atomic-resolution images formed by TDS in a low-order zone axis. Subsequently, HAADF STEM has been positively used to analyze crystal and defect structures in many materials, as shown in Refs. 9–14.

There are two basic methods about the calculations of HAADF STEM images; the multislice method and the Bethe method. The multislice method can be applied to calculations for various objects, but it requires enormous computing time because the whole calculation in the STEM mode has to perform the integration of scattering intensities over a HAADF detector, again and again at each probe position. Most calculations have been carried out only using coherent Bragg reflection without TDS, with the exception of works of Hillyard, Loane, and Silcox[6] and Wang and Cowley.[15,16]

The Bethe method describes wave functions in a crystal by three-dimensional (3D) Bloch waves. The method for HAADF STEM images caused by incoherent TDS was originated by Pennycook and Jesson,[17] and that caused by coherent Bragg reflection was done by Nellist and Pennycook.[18] TDS may not be preferential in a HAADF STEM image of a crystal having a small Debye-Waller factor or a thin thickness even if they are recorded with an ADF detector having a higher inner angle. The contributions of both the incoherent TDS and the coherent Bragg reflections have to be taken into account for HAADF STEM imaging of such a crystal. When images are recorded with a detector having a lower inner angle, the contribution of the coherent Bragg reflections becomes larger. Therefore for quantitative analysis of HAADF STEM images it is desired to develop a method that takes simultaneously both effects into account and calculates the images quickly.

Recently, we have studied As-doped Si by HAADF STEM with the aid of image simulation, and obtained the quantitative 2D distribution of As atoms at atomic resolution.[19] Atomic-resolution HAADF STEM has also been performed for a $SrTiO_3$ ceramic condenser which has a Bi diffusion layer near the grain boundary, and analyzed the Bi concentration in every atomic column.[10] Very recently, we have carried out through-focal HAADF STEM observations of [011]-orientated Si.[20] Artificial bright spots were found on no atomic columns along the electron beam, in some images, and the appearance of these artificial spots was accounted for by the simulation. The effects of aperture size and defocus of a probe-forming lens, both of which determine the shape of the probe, and the effect of the distortion influencing the Bloch wave field of channeling electrons on the HAADF-image intensity were discussed in terms of dynamical effect.[11] From these studies, however, we have reached a conclusion that the image simulations are indispensable for quantification of experimental HAADF STEM images and as such provides a valuable compositional analysis for every atomic column along the incident beam.

In this paper, a method is established for HAADF-STEM

 ©2001 The American Physical Society

image calculations, in which both elastic Bragg reflections and TDS are incorporated as shown in Sec. II. By comparison between experimental and simulated results, the validity and accuracy of the method are critically examined in Sec. III, and the conclusion is finally given in Sec. IV.

II. THEORY

A. Probe function

The coherent convergent probe intensity or probe function $P(\mathbf{R},\mathbf{R}_0)$ at $\mathbf{R}$ on an object surface can be written by superposition of plane waves modulated by the lens aberration function $W(\mathbf{K}_\parallel)$:

$$P(\mathbf{R},\mathbf{R}_0)=\left|\int_{\text{probe}}\exp\{i\mathbf{K}_\parallel\cdot(\mathbf{R}-\mathbf{R}_0)\}\exp\{iW(\mathbf{K}_\parallel)\}d\mathbf{K}_\parallel\right|^2, \tag{1}$$

where $\mathbf{R}_0$ is the center of the incident probe, and $\mathbf{K}_\parallel$ the transverse component of the partial incident plane wave. The lens aberration function $W(\mathbf{K}_\parallel)$ is given by

$$W(\mathbf{K}_\parallel)=\pi\lambda|\mathbf{K}_\parallel|^2\left(\Delta f+\frac{1}{2}C_s\lambda^2|\mathbf{K}_\parallel|^2\right), \tag{2}$$

with defocus Δf, wavelength λ, and spherical aberration C_s.

B. Calculation of ADF STEM image due to coherent Bragg reflection

Nellist and Pennycook[18] proposed an instructive algorithm of HAADF STEM imaging due to coherent Bragg reflection based on the 3D Bloch waves, where absorption, higher order Laue zone (HOLZ) reflections, and the lens aberration function are neglected. The Bloch wave theory can reveal physical pictures of image formation, although it may not be a good way because of the difficulty of dealing with defects. First of all, the method is extended so as to include the effect of the lens aberration function using a matrix form where the relation between the incident beam and the transmitted beam is connected with a transfer matrix. The wave function at $\mathbf{r}(x,y,z)$ in a crystal, formed by a probe located at surface $\mathbf{R}_0$, can be written by

$$\Psi(\mathbf{R}_0,\mathbf{K}_\parallel,\mathbf{r})=\int d\mathbf{K}_\parallel A(\mathbf{K}_\parallel)\sum_i\sum_g \varepsilon^i(\mathbf{K}_\parallel,\mathbf{R}_0)C_g^i(\mathbf{K}_\parallel)\times\exp[i\{(\mathbf{K}_\parallel+\mathbf{g})\cdot\mathbf{R}+k_z^i z\}], \tag{3}$$

where $\varepsilon^i(\mathbf{K}_\parallel,\mathbf{R}_0)$ are the excitation amplitudes for branch i and $C_g^i(\mathbf{K}_\parallel)$ the Bloch wave coefficients for Bragg reflections $\mathbf{g}$. The aperture function $A(\mathbf{K}_\parallel)$ is defined by

$$A(\mathbf{K}_\parallel)=\begin{cases}1 & |\mathbf{K}_\parallel|\leqslant|\mathbf{K}|\sin(\alpha),\\ 0 & \text{otherwise,}\end{cases}$$

where α is a semiangle of an aperture.

By the straightforward approximation, the boundary condition on an entrance surface $(z=0)$ gives rise to the following matrix form:

$$\begin{bmatrix}\varepsilon^1(\mathbf{K}_\parallel,\mathbf{R}_0)\\ \varepsilon^2(\mathbf{K}_\parallel,\mathbf{R}_0)\\ \varepsilon^3(\mathbf{K}_\parallel,\mathbf{R}_0)\\ \vdots\end{bmatrix}=\exp(-i\mathbf{K}_\parallel\cdot\mathbf{R}_0)\times\exp\{iW(\mathbf{K}_\parallel)\}\cdot\tilde{C}^{-1}(\mathbf{K}_\parallel)\cdot\begin{bmatrix}1\\0\\0\\ \vdots\end{bmatrix}, \tag{4}$$

where $\tilde{C}^{-1}(\mathbf{K}_\parallel)$ is the inverse matrix of the eigenvector. By the exit boundary condition on a bottom $(z=t)$, the transmission coefficients are expressed as

$$\begin{bmatrix}T_0(\mathbf{K}_\parallel,\mathbf{R}_0,t)\\ T_g(\mathbf{K}_\parallel,\mathbf{R}_0,t)\\ \vdots\end{bmatrix}=\exp(-iK_z t)\cdot\tilde{C}(\mathbf{K}_\parallel)\cdot\tilde{\Gamma}(\mathbf{K}_\parallel,t)\cdot\begin{bmatrix}\varepsilon^1(\mathbf{K}_\parallel,\mathbf{R}_0)\\ \varepsilon^2(\mathbf{K}_\parallel,\mathbf{R}_0)\\ \vdots\end{bmatrix}, \tag{5}$$

where the matrix element $\{\tilde{\Gamma}(\mathbf{K}_\parallel,t)\}_{i,j}=\exp(ik_z^i t)\delta_{i,j}$.

The transmitted wave is expressed by integration over $\mathbf{K}_\parallel$:

$$\Psi(\mathbf{R}_0,\mathbf{K}_\parallel,\mathbf{R},t)=\int A(\mathbf{K}_\parallel)\sum_g T_g(\mathbf{K}_\parallel,\mathbf{R}_0,t)\times\exp[i\{(\mathbf{K}_\parallel+\mathbf{g})\cdot\mathbf{R}\}]d\mathbf{K}_\parallel. \tag{6}$$

Then, the wave function in the real space is transformed into a diffraction plane:

$$\bar{\Psi}(\mathbf{R}_0,\mathbf{K_f},t)=\sum_g A(\mathbf{K_f}-\mathbf{g})T_g(\mathbf{K_f}-\mathbf{g},\mathbf{R}_0,t). \tag{7}$$

The intensity of the transmitted waves $I_{\text{ADF-STEM}}(\mathbf{R}_0,t)$, encountering the annular detector whose range is restricted from K_{in} to K_{out}, can be calculated by

$$I_{\text{ADF-STEM}}(\mathbf{R}_0,t)=\int D(\mathbf{K_f})\left|\sum_g A(\mathbf{K_f}-\mathbf{g})T_g(\mathbf{K_f}-\mathbf{g},\mathbf{R}_0,t)\right|^2 d\mathbf{K_f}, \tag{8}$$

with

$$D(\mathbf{K_f})=\begin{cases}1 & K_{\text{in}}\leqslant|\mathbf{K_f}|\leqslant K_{\text{out}},\\ 0 & \text{otherwise.}\end{cases}$$

It should be noted that the intensity of an ADF STEM image, ascribed to coherent Bragg reflection, depends on the intensity of wave function at the exit surface, and therefore the intensity of an atomic column is expected to change through thickness, like thickness fringes.

The Fourier transform of Eq. (8) with respect to $\mathbf{R}_0$ is carried out using spatial frequency $\mathbf{Q}$:

$$\bar{I}_Q(t)=\int\sum_g D(\mathbf{K_f})A(\mathbf{K_f}-\mathbf{g})A^*(\mathbf{K_f}-\mathbf{g}+\mathbf{Q})\times\exp[i\{W(\mathbf{K_f}-\mathbf{g})-W(\mathbf{K_f}-\mathbf{g}+\mathbf{Q})\}]\times T'_g(\mathbf{K_f}-\mathbf{g},t)T'^*_{g-Q}(\mathbf{K_f}-\mathbf{g}+\mathbf{Q},t)d\mathbf{K_f}, \quad (9)$$

where $T'_g(\mathbf{K_f},t)$ express the transmission coefficients excluding the effects of the lens aberation and probe position. Equation (9) can be rewritten with $\mathbf{K}_\parallel=\mathbf{K_f}-\mathbf{g}$;

$$\bar{I}_Q(t)=\int\sum_g A(\mathbf{K}_\parallel)A^*(\mathbf{K}_\parallel+\mathbf{Q})D(\mathbf{K}_\parallel+\mathbf{g})\times\exp[i\{W(\mathbf{K}_\parallel)-W(\mathbf{K}_\parallel+\mathbf{Q})\}]T'_g(\mathbf{K}_\parallel,t)\times T'^*_{g-Q}(\mathbf{K}_\parallel+\mathbf{Q},t)d\mathbf{K}_\parallel. \quad (10)$$

Finally, the intensity as a function of $\mathbf{R}_0$ is given by inverse Fourier transformation with respect to $\mathbf{Q}$:

$$I_{\text{ADF-STEM}}(\mathbf{R}_0,t)=\sum_Q \hat{I}_Q(t)\exp(-i\mathbf{Q}\cdot\mathbf{R}_0). \quad (11)$$

C. Absorption and TDS calculation through the optical potential

It takes an extremely long computing time to calculate a full HAADF STEM image including simultaneously both incoherent TDS and coherent Bragg scattering. Although there are quantitative analyses of TDS that have used statistical averages over atomic displacements and phases of phonon scattering,[21,22] we propose the following two-step calculation using two kinds of optical potentials. First, we take the Fourier components of optical potential of TDS:[23–25]

$$V'_{g,(\mathrm{TDS})}=\frac{\hbar^2}{2m_0}\frac{4\pi}{\Omega}\sum_\kappa \exp(-i\mathbf{g}\cdot\mathbf{r}_\kappa)f'_\kappa(\mathbf{s})\exp(-M_\kappa s^2), \quad (12)$$

where Ω is the unit-cell volume, $\mathbf{r}_\kappa$ is the lattice position of k atom. $s=|\mathbf{s}|=|\mathbf{g}|/4\pi$ and M_κ is the Debye-Waller factor of κ atom. The absorption form factor $f'_\kappa(\mathbf{s})$ derived from the Einstein model can be defined in terms of the elastic form factors:

$$f'_\kappa(s)=\frac{2h}{\beta m_0 c}\int d^2\mathbf{s}' f_\kappa(|\mathbf{s}'|)f_\kappa(|\mathbf{s}-\mathbf{s}'|)\times[1-\exp\{-2M_\kappa(s'^2-\mathbf{s}\cdot\mathbf{s}')\}]. \quad (13)$$

Since the absorption potential of TDS, $V'^{\,\mathrm{all}}_{g,(\mathrm{TDS})}$, can be derived from $f'_\kappa(s)$, which is calculated by the integration of Eq. (13) over all the area, the total absorption potential is given by

$$V'^{\,\mathrm{all}}_g=V'^{\,\mathrm{all}}_{g,(\mathrm{TDS})}+V^{\mathrm{plasmon}}\delta_{g,0}+V^{\mathrm{core}}_g, \quad (14)$$

where $\delta_{g,0}$ are Kroneckers delta, and V^{plasmon} and V^{core}_g are absorption potentials of the plasmon loss and core loss, respectively. The wave function $\Psi(\mathbf{R}_0,\mathbf{K}_\parallel,\mathbf{r})$ in Eq. (3) is calculated by using this optical potential $V'^{\,\mathrm{all}}_g$, and thereby the total intensity of transmitted electrons $I_{\mathrm{all}}(\mathbf{R}_0)$ reduced by the absorption due to TDS over all scattering angle, the plasmon loss and the core loss, is obtained from Eq. (11).

Next, in order to evaluate the intensity of TDS electrons collected with the annular detector, the following optical potential $V'^{\,\mathrm{ex}}_{g,(\mathrm{TDS})}$, is introduced as

$$V'^{\,\mathrm{ex}}_{g,(\mathrm{TDS})}=\frac{\hbar^2}{2m_0}\frac{4\pi}{\Omega}\sum_\kappa \exp(-i\mathbf{g}\cdot\mathbf{r}_k)\{f'^{<\mathrm{detector}}_\kappa(\mathbf{s},M)+f'^{>\mathrm{detector}}_\kappa(\mathbf{s},M)\}\exp(-M_\kappa s^2), \quad (15)$$

where absorption form factors for TDS over angle ranges lower than the inner detector angle and that higher than the outer detector angle are defined as

$$f'^{<\mathrm{detector}}_\kappa(s)=\frac{2h}{\beta m_0 c}\int_{<\mathrm{detector}} d^2\mathbf{s}' f_\kappa(|\mathbf{s}'|)f_\kappa(|\mathbf{s}-\mathbf{s}'|)\times[1-\exp\{-2M_\kappa(s'^2-\mathbf{s}\cdot\mathbf{s}')\}], \quad (16)$$

and

$$f'^{>\mathrm{detector}}_\kappa(s)=\frac{2h}{\beta m_0 c}\int_{>\mathrm{detector}} d^2\mathbf{s}' f_\kappa(|\mathbf{s}'|)f_\kappa(|\mathbf{s}-\mathbf{s}'|)\times[1-\exp\{-2M_\kappa(s'^2-\mathbf{s}\cdot\mathbf{s}')\}]. \quad (17)$$

Replacing $V'^{\,\mathrm{all}}_g$ in Eq. (14) with $V'^{\,\mathrm{ex}}_g$, we calculate $I_{\mathrm{ex}}(\mathbf{R}_0)$, where electrons inelastically scattered only outside of the detector are considered as absorbers. Then, the total intensity $I^{\mathrm{detector}}_{\mathrm{TDS}}(\mathbf{R}_0)$ collected with the annular detector is simply calculated by

$$I^{\mathrm{detector}}_{\mathrm{TDS}}(\mathbf{R}_0)=I_{\mathrm{ex}}(\mathbf{R}_0)-I_{\mathrm{all}}(\mathbf{R}_0). \quad (18)$$

It may be noted that the wave function calculated by Eq. (15) and used for the estimation of $I_{\mathrm{ex}}(\mathbf{R}_0)$ is not equal to the exact wave function of elastic scattered electrons in a crystal, which is used in the Pennycook and Jesson's method[17] (hereafter abbreviated to the PJ method), because it is evaluated taking no account of a partial absorption due to the electrons scattered onto the detector. The present approach is also based on the simple kinematic approximation, where once inelastically scattered electrons suffer neither the coherent nor incoherent scattering and which is reasonable in a thinner crystal as suggested by Otsuki[26] and is also used in the PJ method. Equation (18) is thus available only for thin crystals.

We do not use the high angle approximation, which is used in the PJ method, so that our method can be used for not only higher but also lower angle ranges. In the strict sense, current flow must be calculated instead of intensity, but the difference can be neglected in the first approximation.[27]

III. RESULTS AND DISCUSSION

In Figs. 1(a)–(c) through-focal experimental HAADF STEM images are reproduced from our previous paper.[20] The images are of a [011]-oriented Si crystal 91 nm thick and

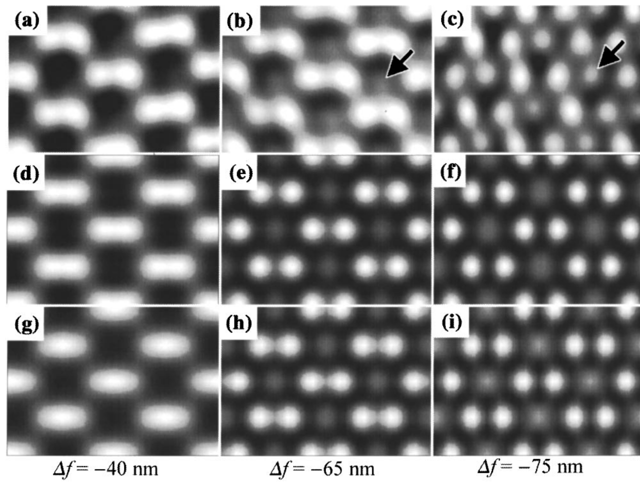

FIG. 1. (a)–(c) Experimental through-focal HAADF STEM images of a [011]-oriented Si crystal 91 nm thick (from Ref. 20). (d)–(f) The corresponding calculated images using the present method. (g)–(i) Those calculated using Pennycook and Jesson's method (PJ method). Artificial spots, marked by arrowheads, appear in (b) and (c).

were noise filtered. They were recorded using a 60–160-mrad annular detector and a lens aperture of a semiangle of $\alpha = 12$ mrad in a JEM-2010F-TEM/STEM. The corresponding calculated images using the present method and the PJ method are shown in Figs. 1(d)–(f) and 1(g)–(i), respectively. The atomic scattering factor proposed by Weickenmeier and Kohl[28] and a Debye-Waller factor of 0.0045 nm^2 in previous references[29,30] were used for both calculations. The $V^{\rm plasmon}\delta_{g,0} + V_0^{\rm core}$ was fixed to be 0.476 eV.[24] The other components of core loss $V_g^{\rm core}$ were neglected because the inelastic scattering processes are insignificant.

Defocus steps between the calculated images exactly agree with the experimental ones which were evaluated from the steps of the objective-lens current knob. Characteristic atomic-resolution images are seen: unresolved bright spots in the dumbbell at an underfocus of $\Delta f = -40$ nm, and the clearly resolved dumbells and artificial spots[20] in the centers of sixfold structures at $\Delta f = -65$ and -75 nm. The experimental images are slightly deformed and show a little deviation from regular bright spot positions, which may be due to instability of the detector, mechanical vibration, current fluctuations, and so on. This is one of the disadvantages of scanning probe techniques. In any case, the calculated images by both methods are almost the same and reproduce the corresponding experimental images satisfactorily. Furthermore, the coincidence between the experimental and simulated images confirms adequacy of the simple kinematic approximation for HAADF STEM.

Figure 2 shows how the thickness affects total HAADF STEM intensities over rectangles with an area of 46×5.6 nm which were measured with the 36–96-mrad detector. The observed data are from Ref. 31. The experimental curve rises gradually with increasing thickness and levels off at 100 nm. For convenience, all the intensity curves are normalized to be a unit at a thickness of 120 nm. The intensities were calculated using the PJ method and the present method.

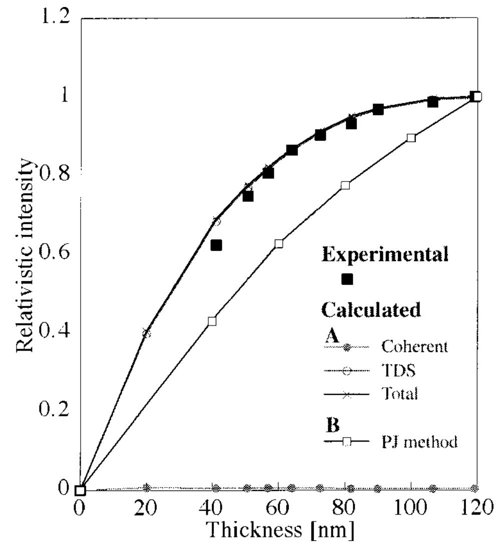

FIG. 2. Thickness dependence of HAADF STEM intensity of [011] Si crystal, using a 36–96-mrad detector. Experimental intensities, denoted by solid squares, are reproduced from Ref. 31. Calculated intensities of coherent Bragg reflection, TDS, and total of both, using the present method (A), are denoted by solid circles, open circles, and crosses, respectively. Calculated intensities using the PJ method (B) are denoted by open squares.

The latter calculation gives the coherent scattering, the incoherent TDS, and the total of both, separately. The intensity of the coherent elastic Bragg reflection can be neglected, and that the total intensity calculated by the present method agrees rather better with the experimental intensity than that by the PJ method, in spite of the approximation in Eq. (15). It also shows that the present approach can be validly used for quantitative analysis of HAADF STEM images of Si

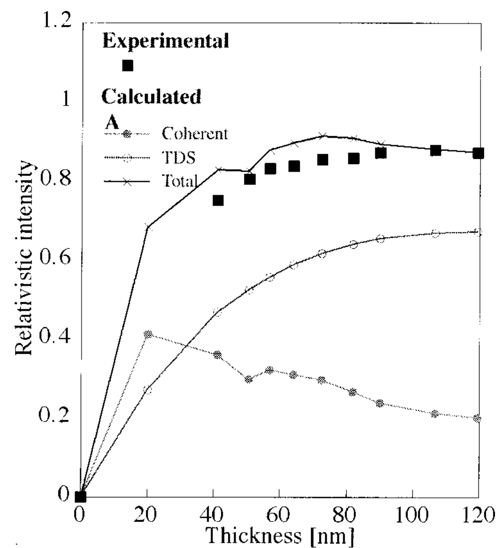

FIG. 3. Thickness dependence of MAADF STEM intensity of [011] Si crystal, using a 18–48-mrad detector. Experimental intensities, denoted by solid squares, are reproduced from Ref. 31. Calculated intensities of coherent Bragg reflection, TDS, and the total of both, using the present method (A), are denoted by solid circles, open circles, and crosses, respectively.

crystals up to 120 nm thick at least.

Figure 3 depicts results similar to those in Fig. 2, except that they were measured or calculated using the 18–48-mrad detector. It is seen that experimental intensity increases with increasing thickness until 40 nm and then becomes flat with a slight fluctuation. Since the PJ method does not calculate the coherent Bragg reflection, it was excluded from the comparison. The total intensity curve calculated by the present method is a satisfactory agreement with the experiment curve. In the middle angle (MA) ADF STEM, the contribution of the coherent Bragg reflection is almost the same order as that by the TDS, although it decreases with increasing thickness, exhibiting a dynamical effect. The decrease of the coherent scattering is ascribed to the absorption, which causes the decrease of the gradient in the TDS curve.

It is be noted that even in HAADF STEM, the coherent scattering must be considered when an annular detector involves many CBD disks on ZOLZ and it works effectively for a crystal having a smaller Debye-Waller factor.

IV. CONCLUSIONS

A different method, using two kinds of optical potentials for TDS, has been proposed for ADF STEM image simulation, which contains calculations for the coherent elastic Bragg reflection and the incoherent TDS. The method reduces the computing time of HAADF STEM images drastically to about one-tenth of that required for the PJ method. The simulations by the present method interpret satisfactorily the experimental focus dependence of atomic-resolution HAADF STEM images, and also the experimental thickness dependence of HAADF STEM intensity and that of MAADF STEM intensity, which includes the dynamical effect of the coherent scattering. Thus the preset method enables us to make a comparison between experimental and simulated HAADF STEM images in a short time as a routine. It has also been confirmed that the simple kinematic approximation for TDS can be used for quantitative analysis of HAADF STEM images up to the thicker area of a sample.

ACKNOWLEDGMENTS

The authors would like to thank Dr. K. Kambe, Germany, for his valuable discussion and useful comments. Discussion with Dr. Y. Kikuchi, Dr. Y. Kotaka, and Dr. M. Kawasaki was extremely valuable.

[1] M. Issacson, D. Kopf, M. Utlaut, N. W. Parker, and A. V. Crewe, Proc. Natl. Acad. Sci. U.S.A. **74**, 1802 (1977).

[2] A. Howie, J. Microsc. **117**, 11 (1979).

[3] E. J. Kirkland, R. F. Loane, and J. Silcox, Ultramicroscopy **23**, 77 (1987).

[4] S. J. Pennycook and D. E. Jesson, Phys. Rev. Lett. **64**, 938 (1990).

[5] R. F. Loane, P. Xu, and J. Silcox, Ultramicroscopy **40**, 77 (1992).

[6] S. Hillyard, R. F. Loane, and J. Silcox, Ultramicroscopy **49**, 14 (1993).

[7] S. Hillyard, R. F. Loane, and J. Silcox, Ultramicroscopy **52**, 325 (1993).

[8] S. Hillyard and J. Silcox, Ultramicroscopy **58**, 6 (1995).

[9] S. J. Pennycook and P. D. Nellist, *Impact of Electron and Scanning Probe Microscopy on Materials Research* (Kluwer Academic, Dordrecht, 1999), pp. 161–207.

[10] M. Kawasaki, T. Yamazaki, S. Sato, K. Watanabe, and M. Shiojiri, Philos. Mag. A **81**, 245 (2001).

[11] T. Yamazaki, K. Watanabe, A. Recnik, M. Ceh, M. Kawasaki, and M. Shiojiri, J. Electron Microsc. **49**, 753 (2000).

[12] S. C. Anderson, C. R. Birkeland, G. R. Antist, and D. J. H. Cockayne, Ultramicroscopy **69**, 83 (1997).

[13] K. Mitsuishi, M. Kawasaki, M. Takeguchi, and K. Furuya, Phys. Rev. Lett. **82**, 3082 (1999).

[14] K. Saitoh, T. Yokosawa, M. Tanaka, and A. P. Tsai, J. Electron Microsc. **48**, 105 (1999).

[15] Z. L. Wang and J. M. Cowley, Ultramicroscopy **31**, 437 (1989).

[16] Z. L. Wang and J. M. Cowley, Ultramicroscopy **32**, 275 (1990).

[17] S. J. Pennycook and D. E. Jesson, Ultramicroscopy **37**, 14 (1991).

[18] P. D. Nellist and S. J. Pennycook, Ultramicroscopy **78**, 111 (1999).

[19] T. Yamazaki, K. Watanabe, Y. Kikuchi, M. Kawasaki, I. Hashimoto, and M. Shiojiri, Phys. Rev. B **61**, 13 833 (2000).

[20] K. Watanabe, T. Yamazaki, Y. Kikuchi, Y. Kotaka, M. Kawasaki, I. Hashimoto, and M. Shiojiri, Phys. Rev. B **63**, 085316 (2001).

[21] R. F. Loane, P. Xu, and J. Silcox, Acta Crystallogr., Sect. A: Found. Crystallogr. **A47**, 267 (1991).

[22] C. Dinges, A. Berger, and H. Rose, Ultramicroscopy **60**, 49 (1995).

[23] C. R. Hall and P. B. Hirsch, Proc. R. Soc. London, Ser. A **286**, 158 (1965).

[24] G. Radi, Acta Crystallogr., Sect. A: Found. Crystallogr. **A26**, 41 (1970).

[25] D. M. Bird and O. A. King, Acta Crystallogr., Sect. A: Found. Crystallogr. **A46**, 202 (1990).

[26] Y. Otsuki, *Charged Beam Interaction with Solids* (Taylor and Francis, New York, 1983).

[27] L. J. Allen and C. J. Rossouw, Phys. Rev. B **42**, 11 644 (1990).

[28] A. Weickenmeier and H. Kohl, Acta Crystallogr., Sect. A: Found. Crystallogr. **A47**, 590 (1991).

[29] C. J. Rossouw, P. Spellward, D. D. Perovis, and D. Cherns, Philos. Mag. A **69**, 255 (1994).

[30] K. Nishio, T. Isshiki, and M. Shiojiri, J. Electron Microsc. **49**, 607 (2000).

[31] Y. Kotaka and K. Watanabe (unpublished).